Modeling the optical properties of self-organized arrays of liquid crystal defects

Delphine Coursault,[1,2] **Bicher Haj Ibrahim,**[3] **Laurent Pelliser,**[1,2] **Bruno Zappone,**[4] **Antonello de Martino,**[3] **Emmanuelle Lacaze,**[1,2,*] **Bruno Gallas**[1,2,*]

[1] *CNRS, UMR7588, Institut des NanoSciences de Paris (INSP), 4 place Jussieu, F-75005, Paris, France*

[2] *Sorbonne Universités, UPMC Univ Paris 06, UMR7588, Institut des NanoSciences de Paris (INSP), 4 place Jussieu, F-75005, Paris, France*

[3] *Laboratoire de Physique des Interfaces et Couches Minces (LPICM), CNRS UMR 7647, Ecole polytechnique, 91128, Palaiseau, France*

[4] *CNR-IPCF, Liquid Crystal Laboratory, Università della Calabria, cubo 33/B, Rende, 87036, Italy*

*emmanuelle.lacaze@insp.jussieu.fr; *bruno.gallas@insp.jussieu.fr*

Abstract: Local full Mueller matrix measurements in the Fourier plane of a microscope lens were used to determine the internal anisotropic ordering in periodic linear arrays of smectic liquid crystal defects, known as 'oily streaks'. We propose a single microstructure-dependent model taking into account the anisotropic dielectric function of the liquid crystal that reproduces the smectic layers orientation and organization in the oily streaks. The calculated Mueller matrix elements are compared to the measured data to reveal the anchoring mechanism of the smectic oily streaks on the substrate and evidence the presence of new type of defect arrangement. Beyond the scientific inquiry, the understanding and control of the internal structure of such arrays offer technological opportunities for developing liquid-crystal based sensors and self-assembled nanostructures.

OCIS codes: (260.2130) Ellipsometry and polarimetry; (160.3710) Liquid crystals; (260.1440) Birefringence; (240.1485) Buried interfaces.

References and links

1. O. D. Lavrentovich, "Designing Dupin cyclides in micro and macro worlds," Proc. Nat. Ac. Sc. **110**(1), 5–6 (2013).
2. A. Honglawan and S. Yang, "Directing 3D Topological Defects in Smectic Liquid Crystals and Their Applications as an Emerging Class of Building Blocks," in *Nanoscience with Liquid Crystals*, eds. (Springer International Publishing, 2014), pp.35–68.
3. C. Blanc and M. Kleman, "The confinement of smectics with a strong anchoring," Eur. Phys. J. E **4**, 241–251 (2001).
4. Y. H. Kim, D. K. Yoon, H. S. Jeong, O. D. Lavrentovich, and H.-T. Jung, "Smectic liquid crystal defects for self-assembling of building blocks and their lithographic applications," Adv. Func. Mat. **21**(4), 610–627 (2011).
5. J. M. Ok, Y. H. Kim, H. S. Jeong, H. W. Yoo, , J. H. Kim, M. Srinivasarao, and H. T. Jung,"Control of periodic defect arrays of 8CB (4-n-octyl-4-cyano-biphenyl) liquid crystals by multi-directional rubbing," Soft Mat. **9**(42), 10135–10140 (2013).
6. J. Michel, E. Lacaze, M. Alba, M. de Boissieu, M. Gailhanou, and M. Goldmann, "Optical gratings formed in thin smectic films frustrated on a single crystalline substrate," Phys. Rev. E **70**, 011709 (2004).

7. B. Zappone and E. Lacaze, "Surface–frustrated periodic textures of smectic–a liquid crystals on crystalline surfaces," Phys. Rev. E **78**, 061704 (2008).
8. B. Zappone, C. Meyer, L. Bruno, and E. Lacaze, "Periodic lattices of frustrated focal conic defect domains in smectic liquid crystal films," Soft Mat. **8**, 4318–4326 (2012).
9. D. K. Yoon, M. C. Choi, Y. H. Kim, M. W. Kim, O. D. Lavrentovich, and H.-T. Jung, "Internal structure visualization and lithographic use of periodic toroidal holes in liquid crystals," Nat. Mat. **6**, 866–870 (2007).
10. C Blanc, D Coursault, and E Lacaze, "Ordering nano-and microparticles assemblies with liquid crystals," Liq. Cryst. Rev. **1**, 83 (2013).
11. D. Coursault, J. Grand, B. Zappone, H. Ayeb, G. Lévi, N. Felidj, and E. Lacaze, "Linear self-assembly of nanoparticles within liquid crystal defect arrays," Adv. Mat. **24**, 1461–1465 (2012).
12. J. Milette, S. Relaix, C. Lavigne, V. Toader, S. J. Cowling, I. M. Saez, R. B. Lennox, J. Goodby, and L. Reven, "Reversible long-range patterning of gold nanoparticles by smectic liquid crystals," Soft Mat. **8**(24), 6593–6598 (2012).
13. J. Michel, E. Lacaze, M. Goldmann, M. Gailhanou, M. de Boissieu, and M. Alba, "Structure of smectic defect cores: X-Ray study of 8CB liquid crystal ultrathin films," Phys. Lett. **96**, 027803 (2006).
14. B. Zappone, E. Lacaze, H. Ayeb, M. Goldmann, P. Barois, and M. Alba, "Self-ordered arrays of wall defects and virtual singularities in thin smectic-A films," Soft Mat. **7**, 1161–1167 (2011).
15. B. Haj Ibrahim, S. Ben Hatit, and A. De Martino, "Angle resolved Mueller polarimetry with a high numerical aperture and characterization of transparent biaxial samples," Appl. Opt. **48**(27), 5025–5034 (2009).
16. T. Novikova, P Bulkin, V. Popov, B. Haj Ibrahim, and A. De Martino, "Mueller polarimetry as a tool for detecting asymmetry in diffraction grating profiles," J. Vac. Sci. Technol. **B 29** (5),051804 (2011).
17. L. Li, "Symmetries of cross–polarization diffraction coefficients of gratings," J. Opt. Soc. Am. A **17**(5), 881–887 (2000).
18. Y. G. J. Lau, S. Klein, C. J. P. Newton, and R. M. Richardson, "Surface ordering at the air-nematic interface. Part 2. A spectroscopic ellipsometry study of orientational order," Liq. Cryst. **34**(4), 421–429 (2007).
19. N. Sbai, J. Perriere, B. Gallas, E. Millon, W. Seiler, and M.C. Bernard, "Structural, optical, and electrical properties of epitaxial titanium oxide thin films on $LaAlO_3$ substrate," J. Appl. Phys. **104**, 033529 (2008).
20. M. Schubert, B. Rheinlander, E. Franke, H. Neumann, J. Hahn, M. Rider, and F. Richter, "Anisotropy of boron nitride thin-film reflectivity spectra by generalized ellipsometry," Appl. Phys. Lett. **70**, 1819 (1997).

1. Introduction

Smectic liquid crystals can form ordered patterns of defects [1,2], in 1D or 2D, depending on the symmetry of the underlying substrate [3–5], and the film thickness [6–8]. They have been used as tunable microlens arrays, and may serve as templates for patterning other kind of materials [9, 10]. In particular, it has been recently shown that 1D defects can trap gold nanoparticles and quantum dots [11, 12] leading to oriented monodimensional chains of nanoparticles [11] and opening the route for various assemblies with the most anisotropic properties. In order to finely control the optical properties of the system and understand the trapping phenomenon, a precise study of the structure of the defects becomes necessary.

We focus here on 1D patterns of defects, known as "smectic oily streaks" (Fig.1). Such patterns occur on substrates imposing planar (parallel molecular orientation) unidirectional anchoring to the liquid crystal molecules, whereas air imposes homeotropic anchoring (perpendicular molecular orientation). On crystalline substrates, it has been shown that they are associated with smectic layers bending in quarters of cylinders with axis parallel to the substrate (Fig.1(b)) [6–8]. We are now able to create them on transparent substrates (polymer on glass) for optical applications [11]. Fig.1(a) shows stripes created on polymer substrates, similar to those observed for MoS_2 and mica substrates [6, 7]. The evolution of the stripe period as a function of the film thickness (Fig.1(c)) reveals that they are associated with flattened hemicylinders, again similarly to MoS_2 substrates [6]. We demonstrate here that a combination of ellipsometry, modeling, and optical microscopy is able to precisely resolve the corresponding internal structure.

On crystalline MoS_2 and mica substrates, it has been shown that x-ray diffraction allows to probe the defects associated with the curved smectic layers in the quarters of cylinders [6, 13, 14]. For a given wave-vector transfer ($\vec{q}$) orientation, the integrated scattered intensity

is proportional to the number of smectic layers perpendicular to $\vec{q}$. This allows to determine the distribution of smectic layers rotating between perpendicular and parallel orientation with respect to the substrate. On MoS_2, we have evidenced the replacement of the highly curved smectic layers around the cylinder axis with horizontal flat layers, resulting in "a rotating grain boundary" [13] (Fig.1(b)). The latter is expected to be composed of topological defects, namely linear smectic dislocations, parallel to the hemicylinder axis and distributed along the rotating grain boundary. They may constitute efficient traps for a linear nanoparticle self-assembly. A question remains unanswered: how are these quarters of cylinders connected to the underlying substrates and does the transition area require new kinds of defects? Such defects would thus also play a role in the trapping of nanoparticles.

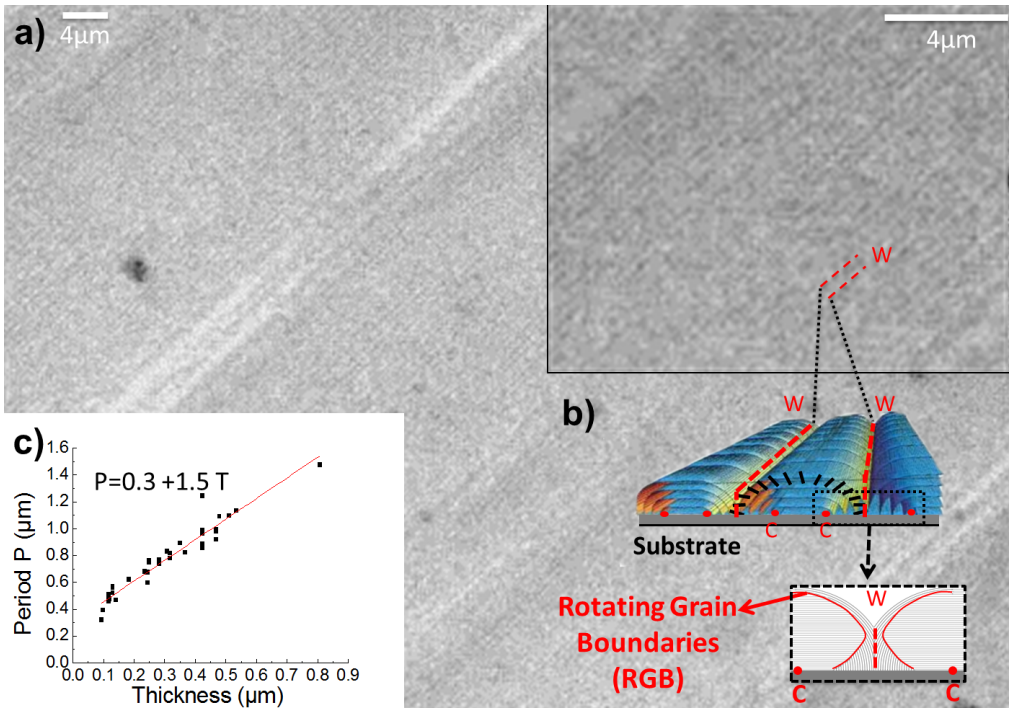

Fig. 1. (a) Polarized optical microscopy image (transmission mode) of a 8CB smectic film with thickness 120 nm on rubbed PVA, showing an array of parallel stripes corresponding to the oily streaks, seen in top view. In insert, Zoom on the (a) picture. (b) Scheme of flattened hemicylinders, with a detail in side view of the area close to the centers of curvature C, including the grain boundary. Hemicylinders are separated by curvature walls W. (c) Period of the hemicylinders (viewed as parallel stripes on (a)) as a function of the film thickness.

2. Ellipsometry modeling

The transition area is expected to be composed of smectic layers perpendicular to the substrate below the quarters of cylinders, and parallel layers below the central part of the flattened hemicylinders. The connection between the two parts requires another new grain boundary (in green in Fig.2(a)). The transition area structure is driven by two factors: on the one hand, the amount of dislocations needed to accommodate the change of direction of the smectic layers across the grain boundary; on the other hand, the orientation dependent anchoring energy of the 8CB molecules on the rubbed polyvinyl alcohol (PVA) substrate, which induces perpendicular

smectic layers. We have considered a model for the internal organization of the oily streaks with two extreme cases for the transition area. A flat grain boundary with a tilt angle of 45° would avoid dislocations to the detriment of smectic layers lying flat on the substrate in the center of the flattened hemicylinders (Fig.2(a) top). Alternatively, the rubbed PVA could be completely covered with vertical smectic layers, forming a grain boundary with a tilt smaller than 45°, which would be favoured by the anchoring mechanism but would introduce a large number of dislocations along the grain boundary (Fig.2(a) bottom). Depending on the energy balance, any intermediate solution may be possible as well.

Ellipsometry is well adapted for the determination of the internal structure of the hemicylinders because of its sensitivity to anisotropy and thickness of thin films. In order to determine the anchoring configuration, we have defined a model, proposed in Fig.2. The internal organization of the smectic layers was simplified by approximating the films as containing domains of constant optical axes orientations as presented in Fig.2(b). Starting from the substrate, there are three sublayers, one corresponding to the transition area and two describing the curved smectic layers around the rotating grain boundary. Each sublayer contains three domains with mirror symmetry with respect to the plane defined by the vertical axis and the longitudinal direction of the flattened hemicylinders (plane (x,y)). The axes of the cartesian referential are defined in Fig.2.

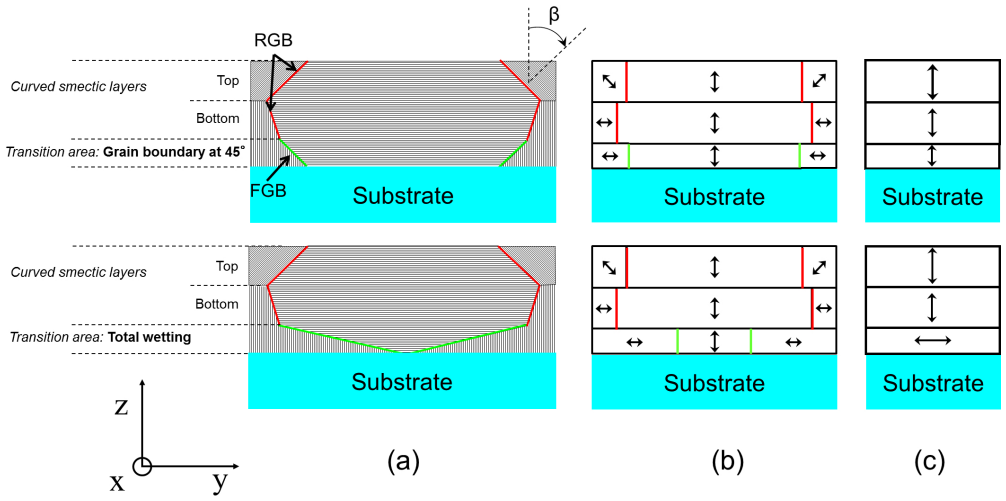

Fig. 2. (a) Simplified models of the internal structure of the oily streaks, shown in side view. The angle β is the orientation of the optic axis of the smectic layers with respect to the substrate. The rotating grain boundary (RGB) is shown in red. The flat grain boundary (FGB) of the transition layer is shown in green. The two extreme models correspond to: the presence of a flat grain boundary in the transition layer with 45° of tilt and the total wetting of the substrate with perpendicular smectic layers covering all the substrate. (b) Equivalent models with domains of constant optic axes directions (indicated by the double arrows). (c) Models with graded birefringence for direct calculations by ellipsometry.

The ellipsometric models outlined above are valid only if (*i*) the light beam is *spatially coherent* over at least one period of the structure, (*ii*) the sample structure is *uniform* (e.g. with thickness, period and other shape parameters remaining constant) over the entire illuminated area and (*iii*) the specularly reflected beam is much more intense than higher diffracted orders which may arise due to the period of the order of 500 nm (Fig.1(c)). If these requirements are

Table 1. Volume fractions of non-horizontal layers and angles of the optic axes for each sublayer of the models of Fig.2.

	Flat grain boundary at 45°		Total wetting of the substrate	
	Fraction of non-horizontal layers	β (°)	Fraction of non-horizontal layers	β (°)
Curved smectic layers (top)	0.28	$\pm$ 45	0.28	$\pm$ 45
Curved smectic layers (bottom)	0.21	90	0.21	90
Transition area	0.33	90	0.69	90

not fulfilled, then the emerging light becomes partially depolarized, compromising the data interpretation by simple ellipsometric models. It is thus important to experimentally assess the absence of depolarization, which is most conveniently achieved by measuring the full Mueller matrix **M** of the sample.

3. Experiments and results

We used a micro-ellipsometry setup allowing local measurements of the Mueller matrix elements at a wavelength of 633 nm on an area with a film of known thickness [15]. The core of the instrument is schematized in Fig.3. A classical (halogen) source is imaged on the back focal plane (BFP) of a microscope objective with an adjustable angular aperture α. A typical bundle of rays, focused on a point A of the BFP and subsequently converted into a parallel beam by the objective, illuminates a circular region of the sample with diameter d proportional to α. The specularly reflected beam is then refocused at point B of the BFP, which is turn imaged on a 2D detector (a CCD camera). As a result, this device provides a 2D image of the angular distribution of the emerging light intensities, where the polar and azimuthal angles (θ,ϕ) of the beam at the sample surface are mapped into radial coordinates $r \propto (\sin\theta,\phi)$. Finally, as the input beam polarization is modulated by a Polarization State Generator (PSG) before reaching the BFP and the emerging beam is also filtered by a Polarization State Analyser (PSA) on its way to the CCD, the device actually provides 16 intensity images with different input and output polarization states, from which the angularly resolved Mueller matrix is eventually extracted. In practice, with a 100 X objective the diameter d of the illuminated area is adjustable from 10 to 50 μm, while the angles (θ,ϕ) cover the range (0°-60°, 0°-360°). Moreover, the angular resolution, of the order of 0.2°, ensures that the beam corresponding to each pixel of the CCD is fully coherent over the illuminated area.

Fig.4(a) presents the Mueller matrix images measured on a 20 μm wide homogeneous region of thickness 170 nm. The thickness was determined using the optical microscopy picture of this region and the measurement of the oily streaks period, 550nm (Fig.1(c)). All elements other than m_{11} are normalized by m_{11}, to decouple the purely polarimetric response from the overall reflectivity given by m_{11}.

For 1D periodic structures aligned along the x axis, with mirror symmetry with respect to the xz plane, the following relations are expected for the Mueller elements, as shown in [16] from the initial work by Li [17] in the Jones formalism:

- for a given set of angles (θ,ϕ),
  $m_{ij} = m_{ji}$ for $(ij) = (12),(14),(24)$
  $m_{ij} = -m_{ji}$ for $(ij) = (13),(23),(34)$
- when ϕ is changed into $-\phi$ or $(180^\circ - \phi)$,
  the elements $m_{ii}, m_{12}, m_{21}, m_{34}, m_{43}$ remain invariant, while the others change sign.

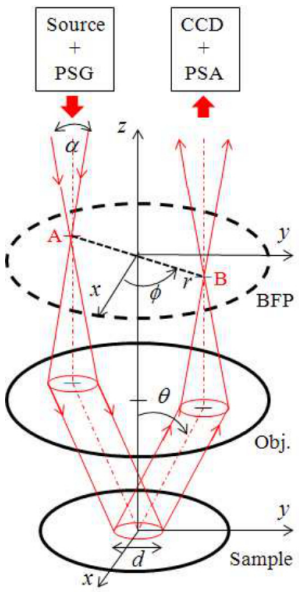

Fig. 3. Scheme of the core of the angularly resolved Mueller micro-polarimeter. BFP : Back Focal Plane of the objective. PSG, PSA : polarization state generator and analyzer. [15, 16]

- when ϕ is a multiple of 90°, $m_{ij} = 0$ for $(ij) = (13), (14), (23), (24)$.

The data shown in Fig.4(a) clearly follow these symmetries. We notice that the unpolarized intensity m_{11} is not constant. An abrupt decrease at angles of incidence above 30° is observed (circle of radius 0.5 in Fig.4(a)), essentially due to a sharp decrease of the sample reflectivity at high incidences. As a result, normalized m_{ij} are clearly much more noisy above 30°. However, due to the linearity of the measurement procedure which uses ratio of intensities, their average values are not affected by the noise, resulting in clearly visible trends even at large angles. In contrast, the depolarization factor Fig.4(b), which remains close to zero below 30°, takes large positive values for larger angles. This effect is due to the evaluation of the depolarization factor which depends quadratically on the Mueller matrix elements. This dependence increases artificially the average value in presence of noise. Finally, the depolarization factor is significant only between 0° and 30°, and its small value in this range clearly confirms that the simple ellipsometric interpretation of the data associated with the models of Fig.2(a) is relevant.

Table 1 summarizes for the model of Fig.2, the values of the volume fractions of non-horizontal smectic layers in each sublayer, and the corresponding orientation β of the optic axis relative to the substrate. In the region of curved smectic layers, the fractions of layers parallel to the substrate and localized in the center of the flattened hemicylinders were determined from geometrical considerations related to x-ray measurements performed for oily streaks on MoS_2 [6], and from the known value of the hemicylinder width, 550nm (Fig.1(c)). We indeed expect that the rotating grain boundary may not vary when the substrate is changed since it is the result of the balance between the elastic energy of curved smectic layers and the grain boundary energy. For the second sublayer, despite the fact that it represents the lower part of the curved smectic layers, we assume the β angle to be of 90° as this area corresponds mainly to smectic layers curving at small angles. In the transition area, we present the fractions for the two extreme cases shown on Fig.2.

The measured Mueller matrix elements were compared to simulations using different multi-

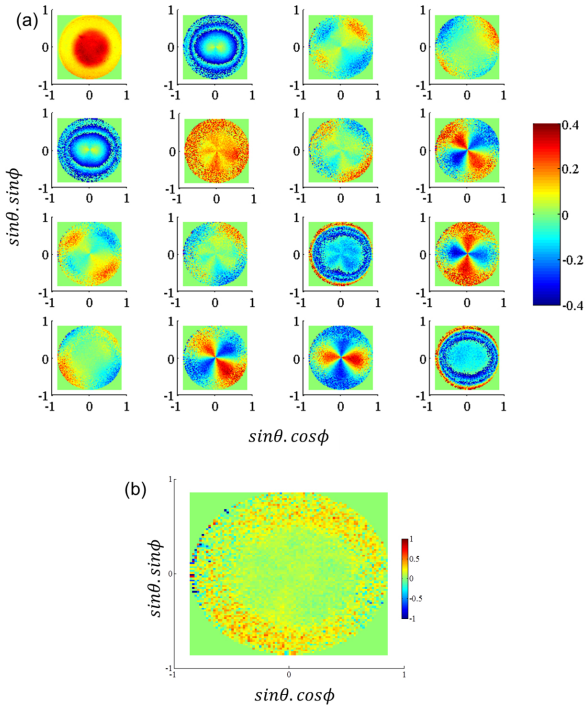

Fig. 4. (a) Measured Mueller matrix images in the BPF, as mapped by the objective ($x = \sin\theta.\cos\phi$, $y = \sin\theta.\sin\phi$) (b) Depolarization factor extracted from these measurements.

layer models. The optical constants of the substrate were those of BK7. The rubbed PVA layer was taken into account as a layer of 10 nm with optical constants of PVA, as measured on a reference sample. It must be noted that no anisotropic optical response could be detected on this reference sample. For the liquid crystal layer, we have used the ordinary and extraordinary optical constants of 8CB taken from [18]. We point out that the thickness of the thin film was not a free parameter. Indeed, as stated above, its value of 170 nm was determined from the oily streaks period of 550 nm observed in the optical microscope on the measured area.

In Fig.2(b), each sublayer is equivalent to a layer with two principal optic axes oriented along the y and z axes, with optical constants to be determined, and one optic axis along x with the ordinary optical constant of 8CB. This yields an equivalent graded biaxial model (Fig.2 (c)). The evaluation of the optical constants along y and z requires first the determination of an equivalent biaxial permittivity tensor for each sublayer of the models of Fig.2 (b). For each domain containing smectic layers with optic axis tilted by an angle β with respect to the substrate, the permittivity tensor expressed in the cartesian referential reads:

$$\varepsilon = \begin{bmatrix} \varepsilon_o & 0 & 0 \\ 0 & \varepsilon_e.\sin^2(\beta)+\varepsilon_o.\cos^2(\beta) & \sin(\beta).\cos(\beta).(\varepsilon_o-\varepsilon_e) \\ 0 & \sin(\beta).\cos(\beta).(\varepsilon_o-\varepsilon_e) & \varepsilon_o.\sin^2(\beta)+\varepsilon_e.\cos^2(\beta) \end{bmatrix}.$$

Then, the optical constants in each sublayer were obtained by averaging the permittivities tensors corresponding to each domain i of orientation β_i in the sublayer, weighted by their respective fractions f_i. A similar procedure has been used for polycrystalline materials for instance [19]. The values of β_i and f_i are given in Table 1. For each sublayer, this yields a permittivity tensor ε_{layer}, which reads in the cartesian referential :

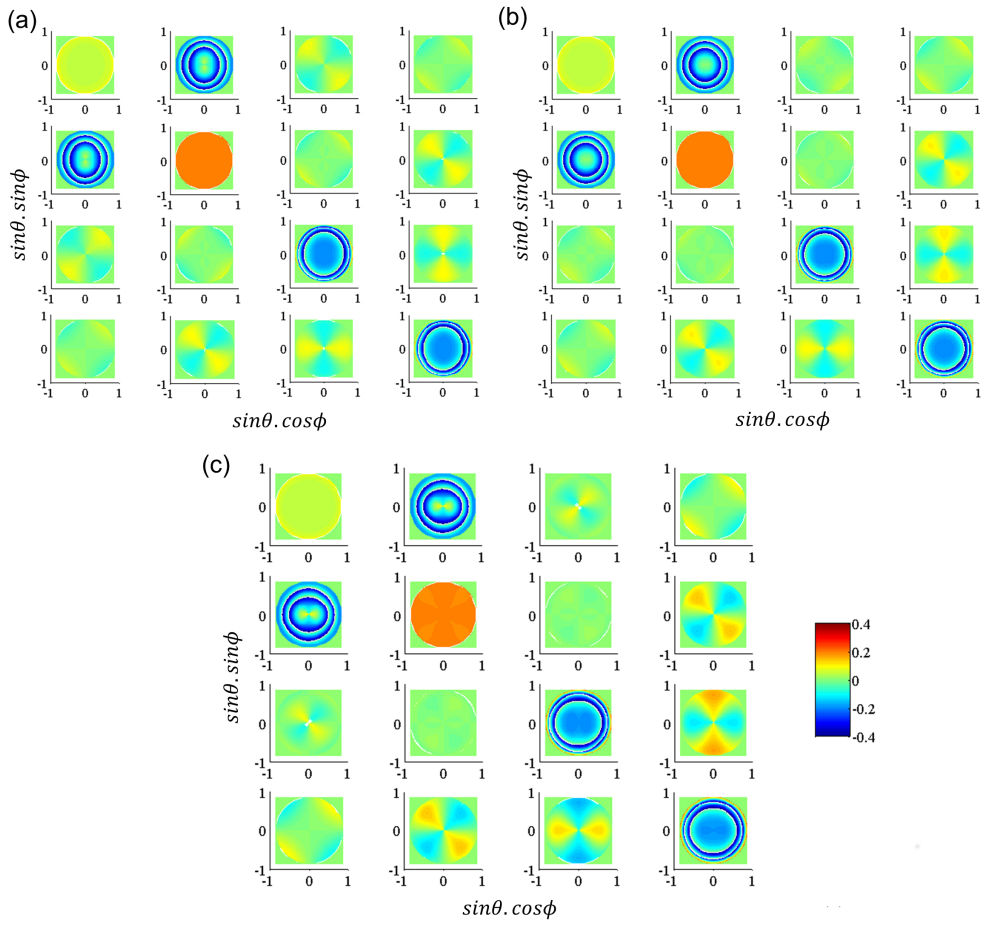

Fig. 5. Mueller matrix elements calculated using (a) a simple biaxial model (b) the graded biaxial model with a flat grain boundary at 45° in the transition area and (c) the graded biaxial model with total wetting of the substrate in the transition area (best adjustment). All elements are plotted to the same scale.

$$\varepsilon_{layer} = \begin{bmatrix} \varepsilon_o & 0 & 0 \\ 0 & \sum_i f_i.(\varepsilon_e.\sin^2(\beta_i) + \varepsilon_o.\cos^2(\beta_i)) & \sum_i f_i.(\sin(\beta_i).\cos(\beta_i).(\varepsilon_o - \varepsilon_e)) \\ 0 & \sum_i f_i.(\sin(\beta_i).\cos(\beta_i).(\varepsilon_o - \varepsilon_e)) & \sum_i f_i.(\varepsilon_o.\sin^2(\beta_i) + \varepsilon_e.\cos^2(\beta_i)) \end{bmatrix}.$$

When the domains are oriented symmetrically with respect to the normal to the surface and in equal proportions, it can be noted that the sum in the off-diagonal elements of ε_{layer} vanishes thanks to the $sin(\beta_i)$ dependence of these elements. These conditions happen when light propagates in the (x,z) plane or the (y,z) plane. As a consequence, this model of averaging does not yield transfer of polarization in these measurement conditions, as expected from the symmetry considerations stated above. The permittivity tensors in the ellipsometer referential are obtained by applying the rotation matrix using the conventional Euler angles. The summation can be extended to a continuous variation of directions as was proposed for instance to reproduce the optical anisotropy of microcrystalline boron nitride where all extraordinary axes were located on a cone [20]. Having defined the equivalent biaxial permittivity tensors for each sublayer, it is then possible to build the graded biaxial medium of Fig.2(c).

In the most straightforward model, we have calculated the averaged fractions of tilted, vertical and horizontal smectic layers, respectively, considering a single layer containing the 9 domains of the "total wetting" structure shown in Fig.2(b) but assuming no vertical organization. It is thus simplified into a simple biaxial model. The response of this single 170 nm thick layer is presented in Fig.5(a). As some Mueller matrix elements inverted signs with respect to the measured ones (see m_{24}, m_{42}, m_{34} and m_{43} for instance), this model can be ruled out. This shows that a superposition of sublayers is necessary. In a second series of adjustments, we have considered curved smectic layers without transition area, thus of total thickness 170 nm. The agreement with the experimental data was bad, leading to the necessity of a transition area in contact with the substrate. We have thus considered in a third step curved smectic layers of thickness 130 nm together with the presence of a transition area of thickness 40 nm. These values were estimated from the results of Fig.1(c). A departure from linearity for a thickness of approximately 130 nm can be observed on the plot of the thickness as a function of the period of the oily streaks. We assume that it corresponds to the minimum thickness necessary to establish the rotating grain boundary in the oily streaks, in agreement with the structural models established from x-ray measurements performed on similar films deposited on MoS_2 [13]. The thickness of the curved smectic layers was then divided in two sublayers of equal thickness of 65 nm, labelled curved smectic layers bottom and curved smectic layers top in Fig.2 and in Table 1. The only remaining unknown parameter was the width on the substrate wetted by vertically oriented smectic layers. This value was adjusted and was allowed to vary between 193 nm corresponding to a flat grain boundary at 45° in the transition area (Fig.2(a)top) and 550 nm corresponding to a total wetting of the substrate (Fig.2(a)bottom). This yields volume fractions of 67 % and 31 % of layers parallel to the substrate in the transition area, respectively (Tab. 1). The adjustment of this volume fraction converged to the total wetting solution even with a starting point corresponding to the flat grain boundary at 45°. Figs.5(b) and 5(c) present the matrix elements calculated using the model with flat grain boundary at 45° (starting point of the adjustment) and the model of total wetting (best result of adjustment), respectively. With a total wetting, a larger contrast in the Muller matrix elements was obtained, closer to experimental measurements, in particular in the off-diagonal elements associated with in-plane anisotropy. The two-fold symmetry of m_{12} and m_{21} was also reproduced.

4. Conclusion

The agreement between simulations and experimental data shows that the model issued from x-ray measurements on crystalline substrates is still valid for glass substrates covered with rubbed PVA. In particular, it confirms the presence of a rotating grain boundary, together with a large

number of layers parallel to the substrate located at the center of the oily streaks hemicylinders. These results yield a comprehensive view for the substrate influence on the oily streaks inner structure. Depending on the anchoring energy of the substrate, we expect variations in the balance with respect to the dislocations energy. This may lead to variations in the angles of the flat grain boundaries within the transitions areas, depending on the underlying substrates. The better agreement obtained for the model of total wetting on PVA substrates, suggests that the anchoring energy between the rubbed PVA and the 8CB is significantly higher than the energy of the dislocations, leading to a large number of dislocations in the tilted grain boundary of the transition area. These dislocations are topological defects, characterized by a disordered core, which may thus constitute a second trapping site for nanoparticles, in addition to the ones distributed along the rotating grain boundary [10].

These results finally evidence the high potential of micro-ellipsometry in combination with x-ray diffraction, for the determination of complex liquid crystal structures.

Acknowledgment

This work was partly supported by the PNANO program of the French national research agency (ANR) through grant ANR-09-Nano-003, Nanodiellipso.